

COVER PAGE

Document downloaded by @DAEL

Sat Nov 28 02:08:56 2026
For personal use

When automatic English translation is provided, only the original document is authentic.
The EAA cannot be held responsible of any translation error

Bibliographical reference

Ultrasound Plane Wave Doppler Quantification Using a Wall-Less Spinal Cord Representative Phantom, D. Lemonnier, J-M. Mac-Thiong and P. Bélanger, Acta Acustica **vol. 104** (Number 1), 2018, pp. 166-173

DOI
https://doi.org/10.3813/AAA.919156

Acta Acustica united with Acustica
Vol. 104 (2018) 166 – 173

Technical and Applied Papers
DOI 10.3813/AAA.919156

Ultrasound Plane Wave Doppler Quantification Using a Wall-Less Spinal Cord Representative Phantom

D. Lemonnier[1,2], J-M. Mac-Thiong[2,3,4], P. Bélanger[1,2]

[1] Ecole de Technologie Supérieure, Department of Mechanical Engineering, 1100 Notre-Dame Ouest Street, Montreal, QC H3C 1K3, Canada. david.lemonnier4@gmail.com

[2] Hôpital du Sacré-Cœur de Montréal Research Center, 5400, Gouin Ouest Boulevard, Montreal, QC H4J 1C5, Canada

[3] Department of Surgery, University of Montreal, 2900, Edouard Montpetit Boulevard, Montreal, QC, H3T 1J4, Canada

[4] Department of Surgery, Sainte Justine Hospital, 3175, chemin de la Côte-Sainte-Catherine, Montreal, QC H3T 1C4, Canada

Summary

Spinal cord injuries are particularly impairing for patients, and can cause significant functional loss. Ultrasonic Doppler imaging is currently being studied as a clinical tool to link vascularization with injury severity. The sensitivity limitation may be improved by using a plane wave algorithm and should thus allow velocity estimation on small vessels with high blood velocities. This study quantifies the efficiency of both the conventional focused and the plane waves algorithms using wall-less phantoms with vessels of diameters close to what is observed in the spinal cord. The design of a wall-less flow phantom with small vessel diameters allowed us to compare the two Doppler sequences in conditions similar to those present in spinal cord imaging. This study focuses on seven vessel diameters ranging from 0.25 mm to 0.7 mm. The blood mimicking fluid flow was controlled using a pump ensuring a mean velocity of 10 cm/s. Using a Region Of Interest (ROI) centered on the maximum value pixel, the Signal-to-Noise Ratio (SNR), the diameter and velocities were calculated from the power Doppler images with both imaging processes. The algorithms' parameters were chosen to ensure the same Doppler sampling frequency, which allowed comparisons. The insonification angle was approximately 25° using a center frequency of 8.3 MHz. The SNR was 13 to 18 dB higher when using plane waves. The focused algorithm consistently overestimated the calculated diameter and underestimated the mean velocities. Higher SNR and more accurate diameters and velocities were obtained when using the plane wave imaging algorithm. This algorithm is therefore of particular interest in spinal cord vascularization measurements.

PACS no. 43.35.Yb, 43.80.Vj

1. Introduction

The spinal cord is a critical tissue in the body, which is rich in nervous terminations. Any alteration in its structure may induce functional loss and neurological defects which may strongly impair patients' lives. In the United States, the incidence of traumatic spinal cord injury (SCI) is estimated to be as high as 65 cases per million [1]. There is therefore great motivation to characterize spinal cord damage in order to predict potential functional recovery and adapt treatments accordingly. As detailed by Martirosyan [2], traumatic SCI involves vascular injury with a specific chronology. Particularly, a link between the severity of an SCI and the alteration of spinal cord blood flow (SCBF) causing posttraumatic ischemia was found by Fehlings [3] and Guha [4], showing a linear decrease in SCBF with an increasing severity of the SCI. Moreover, neurological deficits have been linked to the evolution of the SCBF in monkeys [5].

Magnetic Resonance Imaging (MRI) and Computed Tomography (CT) are commonly used following a SCI [6], and both modalities can be combined with an angiography. These techniques are however not portable, and require the injection of an intravenous contrast agent, following which they may then induce complications during clinical use. Laser Doppler Flowmetry allows the quantification of SCBF using a non-invasive and continuous method, but only provides access to one-dimensional data, and is limited to a depth of approximately 1 mm [7]. Ultrasound imaging represents an alternative method for characterizing soft tissues, and allows real-time calculation of velocities and perfusion detection when used in Doppler mode.

Received 31 October 2016,
accepted 11 December 2017.

© S. Hirzel Verlag · EAA

The human spinal cord blood flow is mainly supplied by one Anterior Spinal Artery (ASA) and two Posterior Spinal Arteries (PSA). Central arteries then branch out from the ASA to the center of the spinal cord, resulting in smaller capillaries, which supply the grey and white matter. The diameter of human spinal arteries ranges between 1 mm and down to 6 µm for the capillaries in the grey matter [8, 9]. However, variations of −50% to +80% have been observed in the PSA diameter of rats [10].

The quantification of blood flow is generally performed with radioactive microspheres, in turn leading to a quantification of the overall spinal cord blood flow. It is however difficult to quantify blood flow per time unit in any specific vessel at a fixed vertebral position. An alternative method is to quantify the blood velocities and the diameter of the arteries, which may be achieved with Doppler ultrasound, but only a few studies describe these velocities in spinal cord arteries. In a human case report [11], the ASA blood velocity for the fourth cervical (C4) position ranges from 6 cm/s to 12 cm/s, and from 1 cm/s to 22 cm/s for the second thoracic (T2) level, depending on the acquisition interval in the cardiac cycle. In dogs, velocities (averaged over 34 animals) from 3.5 cm/s to 5.78 cm/s were obtained for the intraparenchymal arteries [12].

In [13, 14, 15, 16], Doppler ultrasound was implemented on the spinal cord to characterize the segmental arteries or spinal arteries. However, the small diameters of the arteries led to a low sensitivity to blood flow variations. A recently developed ultrasonic Doppler imaging sequence called ultrafast imaging, which uses plane wave emissions [17] could provide a means to overcome the preceding limitations, and has been successfully used to image the cerebral blood flow in rats. In this technique, instead of using focused waves, the entire image is scanned at each emission, with the possibility of defining different angles to obtain a compound image, which reduces the noise. The transmitted energy is higher and the same image quality can be achieved with fewer emissions, thus enhancing sensitivity of images for an equivalent time. This algorithm was also applied in vivo to describe the arteries of the carotid [18, 19] or the heart [20, 21, 22]. However, it is not used for the spinalcord imaging yet, with its specific conditions and limitations described previously.

The objective of this study is to quantify and compare the Doppler image characteristics obtained with a focused and a plane wave algorithm for the specific case of small vessels and high fluid velocities with a spinal cord representative environment. The paper first introduces the method describing the flow phantom design, the experimental setup, the image acquisition and data processing. This is then followed by a description of the results and a discussion.

2. Methods

2.1. Phantom design

Flow phantoms are often used for Doppler ultrasound imaging to quantify the accuracy of an algorithm, usually for quality control purposes. The most common technologies in this regard use a moving string with a controlled speed, a rotating cylinder or a Blood Mimicking Fluid (BMF) flowing inside a fixed diameter vessel. However, in order to get a more realistic configuration and more complex geometries, phantoms can be made using Tissue Mimicking Materials (TMM). Some of these have been suggested for iliac arteries [23], carotid arteries [24, 25], coronary arteries [26], or capillaries [27, 28, 29, 30]. However, particularly for the small vessels, the flow in these phantoms is generally guided with a tube, which can be made of latex or silicon. The vessel wall material causes higher reflection due to acoustic impedance mismatch and can create shadowing cone artifacts [24]. As well, for these vessels, the velocities can be overestimated due to a Doppler spectrum distortion [31].

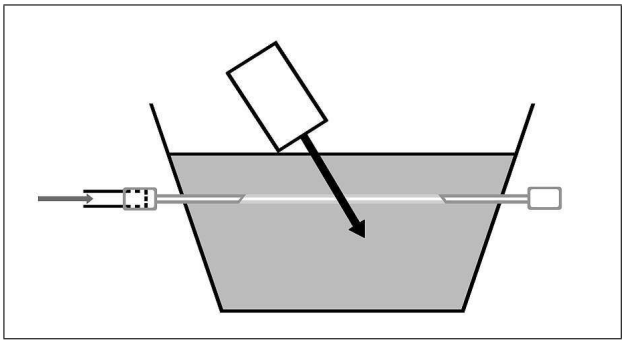

Figure 1. Schematic description of the phantom design. The angle between the flow and the probe orientation is approximately 25°. The BMF enters into the phantom from one guide and goes out though the guide on the other side after flowing inside the TMM in a wall-less cylinder.

In this study, the Doppler flow phantom (Figure 1) was included in a plastic container. A wire with a known diameter was passed through it, guided with two metallic cylinders on either side, and leading to an unsupported length of approximately 2 cm in the middle. Wire diameters of 0.7 mm, 0.6 mm, 0.55 mm, 0.5 mm, 0.35 mm, 0.3 mm and 0.25 mm were used. A liquid tissue mimicking material (TMM) recipe [32] was chosen to fill the container. The human sagittal spinal cord diameter ranges from 10 mm to 2 mm, depending on the vertebral level [33] and as a result, the wire depth was therefore chosen to be approximately 1 cm, simulating potential clinical conditions when assessing the ASA from a posterior approach following a laminectomy. The wire was carefully removed from one guide to obtain a cylinder of the desired diameter in the TMM. The phantoms were left in a refrigerator (T = 4 °C, maximum three days) between the fabrication and experimental acquisition of ultrasonic waves.

The speed of sound and the density of the TMM were calculated for each phantom (Table I). The mass of the phantom was measured with an electronic balance (type L310, Sartorius Laboratory, Goettingen, Germany), and the volume determined by reading the volume difference on a beaker scale (1mL precision) after immersing the phantom in water. The speed of sound in the TMM was calculated by measuring the phantom thickness with

a caliper (CD-6″CSX, Mitutoyo, Aurora, IL, USA), as well as the time-of-flight of the ultrasonic wave travelling through the phantom.

2.2. Experimental setup

The ultrasonic probe was retained with a holder in order to maintain constant imaging conditions. Of particular importance was the angle between the flow and the probe, which was kept constant on any given phantom. This angle was chosen to be approximately 25°, and for each phantom, was determined more precisely by tracing the probe and the guides axis on a picture acquired perpendicular to the probe. The flow was generated from a pump (Masterflex L/S Easy-load II, Cole-Parmer, Vernon Hills, IL, USA) with a constant flow, while the flow was chosen to ensure a fluid velocity of 10 cm/s within each of the phantoms (Table II) to fit with the mean human spinal cord vessels velocities reported in the literature [11]. The blood mimicking fluid (BMF) (Shelley Medical Imaging Technologies, London, ON, Canada) contained 5 µm diameter nylon particles. It was pumped from a small regularly mixed container in order to keep the BMF homogeneous, in a tube with an interior diameter of 0.8 mm (Masterflex L/S 13, Cole-Parmer, Vernon Hills, IL, USA) which was directly connected and glued to one of the phantom's guides in order to avoid leakage.

2.3. Image acquisition

Water was added to the top of the phantoms in order to provide a soft matching layer between the probe and the TMM. Ultrasound imaging was performed using the Verasonics V1 System and the L11-4v transducer (Verasonics, Kirkland, USA), used at a 10 MHz frequency. To ensure flow visualization, as well as a fit with actual spinal cord dimensions, the 64 central elements of the probe were used, corresponding to a length of 19 mm, while the imaging depth was chosen to be 20 mm to hold a complete potential spinal cord. The transducer was in contact with the TMM, and permanently placed perpendicular to the flow to capture transverse images. Measurements were performed at several spatial positions, translating the probe over the surface (keeping the same inclination), in order to characterize the flow at different positions in the 2D Doppler images; the quantification and the flow position in the images were thus uncorrelated. The vessel depth inside the TMM was then always identical, close to the focal depth of the focused wave imaging sequence. For each phantom and for each position, both the focused and the plane wave algorithms were used alternatively, allowing a comparison under the same conditions, and avoiding potential temporal changes in the phantoms.

2.4. Ultrasound algorithms

To allow a direct comparison between the two techniques, the two sequences were acquired with the same Pulse Repetition Frequency (PRF) over the complete image, as detailed by Macé [17]. A summary of the different parameters for the two algorithms is given in Table III. The main difference is the number of stored images, which is almost thirteen times higher for the plane wave sequence.

Table I. Density ρ, speed of sound c and acoustic impedance Z of the test samples. A good agreement is found with the water density value of 1000 kg/m^3 (1.9%). As discrepancies were found with the speed of sound of 1480 m/s (2.7%) in water, the mean value of 1441 m/s was used for the calculations.

	ρ [kg/m^3]	c [m/s]	Z [MRayl]
Sample 1	1027	1422	1.46
Sample 2	995	1438	1.43
Sample 3	1005	1429	1.44
Sample 4	949	1418	1.35
Sample 5	1063	1385	1.47
Sample 6	1074	1424	1.53
Sample 7	1000	1513	1.51
Sample 8	999	1480	1.48
Sample 9	1041	1443	1.50
Sample 10	1040	1458	1.52
Mean	1019	1441	1.47

Table II. Diameters d [mm] used for the Doppler phantoms with the corresponding flows [mL/min], in order to obtain a mean theoretical velocity of (10 cm/s) for every case.

d	0.25	0.30	0.35	0.50	0.55	0.60	0.70
flow	0.29	0.42	0.58	1.18	1.43	1.70	2.31

Table III. Experimental parameters for the sampling frequency equivalent Doppler algorithms (Plane wave and Focused).

	Plane wave	Focused
Wave frequency	10 MHz	10 MHz
Length of the emitted signal	2 cycles	2 cycles
Aperture	64 elements	26 elements
Focal length	–	10 mm
Steering	±5°	–
Imaging depth	19 mm	19 mm
Pulse Repetition Frequency	15380 Hz	15380 Hz
Doppler sampling frequency	3070 Hz	3070 Hz
Number of angles	5	–
Lines in a block	–	5
Number of blocks	–	13
Number of waves	1600	1600
Acquisition time	104 ms	104 ms
Number of images	320	25

Both imaging processes use 1600 emissions with a pulse repetition frequency (PRF) of approximately 15 kHz. The total acquisition length for one image is 104 ms. The signal emitted by the probe is a 10 MHz burst of 2 wavelengths, and the sampling frequency of the data is 25.7 MHz. The Doppler frequency is calculated with the following equation,

$$f_D = \frac{2\, f_0\, v\, \cos(\theta)}{c}, \tag{1}$$

where f_D is the Doppler frequency, f_0 is the frequency of the emitted wave, v is the actual flow velocity, c is the

speed of sound in the medium, and θ is the angle between the transducer and the vessel.

A compounding sequence was performed for plane wave imaging. The most limiting calculation for the Doppler sampling frequency with spinal cord imaging is derived from the central arteries. As they mainly extend parallel to the ultrasound beam, there may be no angle correction to apply in the Doppler equation. The blood velocity projected on the wave propagation axis is then the actual blood velocity and the Doppler frequency shift reaches its maximum.

In a scenario with no angle, and for a maximum blood velocity of 6 cm/s in the dog's central arteries described previously [12], the maximum Doppler frequency would be approximately 780 Hz (1560 Hz with the Nyquist limit). Assuming that these velocities are higher for the human spinal cord, and in accordance with a case report [11], we then set the minimum Doppler frequency limit to 3000 Hz, allowing a plane wave emission sequence using 5 steered beams for one Doppler image, with a sampling frequency of 3070 Hz. The angles were spaced equally between $+5°$ and $-5°$, which is a trade-off between variety in the data and the limitation of the insonified field. To maintain the same Doppler sampling frequency over the whole image, the focused emissions were divided into 13 blocks of 5 columns (4 columns for the first block). For each column, an emitted beam was focused in front of the corresponding element, with a focal length of 10 mm and an F-number of 0.4 (26 active elements). It should be noted that the Doppler data saving is limited to the 64 center elements of the probe, but there is no limitation associated to the wave emission sequence. Therefore, any number of elements can be activated simultaneously to generate the ultrasound wave.

2.5. Signal and image processing

The raw radiofrequency (RF) data were stored after each acquisition, and then used for images reconstructions after the end of the experiments. First, a Time Gain Compensation (TGC) was applied to the RF data to take the attenuation of the phantom into account. Then, a demodulation process was performed, using a 6th order Butterworth low pass filter and decimation. It should be noted that the actual frequency emitted by the probe (and used for the demodulation) was verified using the frequency spectrum of an echo received from a fixed reflector, and was approximately 8.31 MHz. The gap between this value and the nominal frequency of 10 MHz can be explained by the bandwidth of the probe used in this experiment which had a center frequency of 6.43 MHz. The theoretical axial resolution was calculated by halving the pulse length, leading to a value of 0.17 mm.

The In-phase and Quadrature (I/Q) components of the data were then beamformed using the Delay And Sum method, with an F-number of 1.5. A phase rotation correction induced by the I/Q data summation had to be performed. A 70 Hz clutter filter (6th order Butterworth) was applied to the Doppler data. To reduce the noise, a cosine taper window centered on the maximum of the frequency signal was added. The power of the signal was calculated with the square of the filtered I/Q data spectrum values for each pixel, and signed as the difference between the positive part of the frequency spectrum with the negative part. The velocity was finally calculated with an autocorrelation equation.

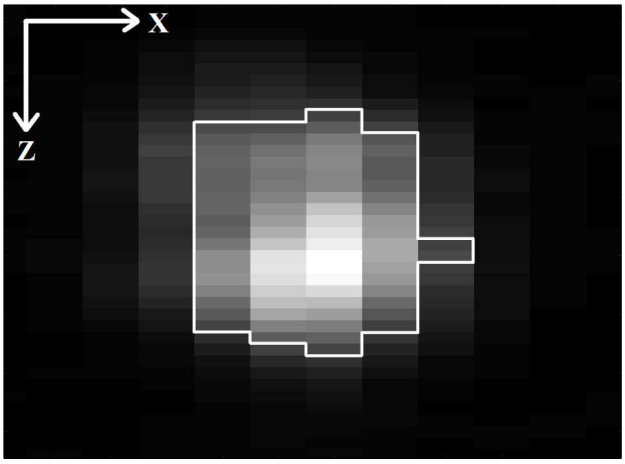

Figure 2. Example of the ROI calculation for one reconstructed image. The maximum pixel was selected manually. Then the neighbours for which the amplitude was higher than -6 dB of the maximum value were selected iteratively until no more pixels were present. The X-axis is along the probe elements, and the Z-axis corresponds to the imaging depth.

2.6. Quantification

In order to compare the efficiency of the two Doppler ultrasound algorithms for a small vessel with a high fluid velocity, the signal-to-noise ratio (SNR), the velocities and the image flow diameter were quantified. Firstly, a region of interest (ROI) was defined for the calculations. As shown in Figure 2, the maximum value pixel in the power Doppler images was manually selected, and then extended to all the neighbors with a value greater than -6 dB of this value. The 6 dB threshold corresponds to the full width at half maximum criterion commonly used in signal processing. All the acquired images had the same number of pixels (158 in the probe length axis or x-axis, 400 in the depth axis or z-axis).

The quantification parameters were then calculated from this defined ROI. The mean velocity is the mean of the values calculated with the autocorrelation equation inside the ROI. As an inclination of approximately $25°$ was used for the probe, the image of a theoretical circle diameter may be slightly distorted in the depth axis. The diameter was then calculated from the maximum ROI length in the X-axis between all the Z-axis positions. Finally, the value of the signal was calculated as the mean of the pixel amplitudes in the Power Doppler image; the noise, which is assumed to be a white noise, as the standard deviation from all the other pixels; and the SNR as the ratio of these two values.

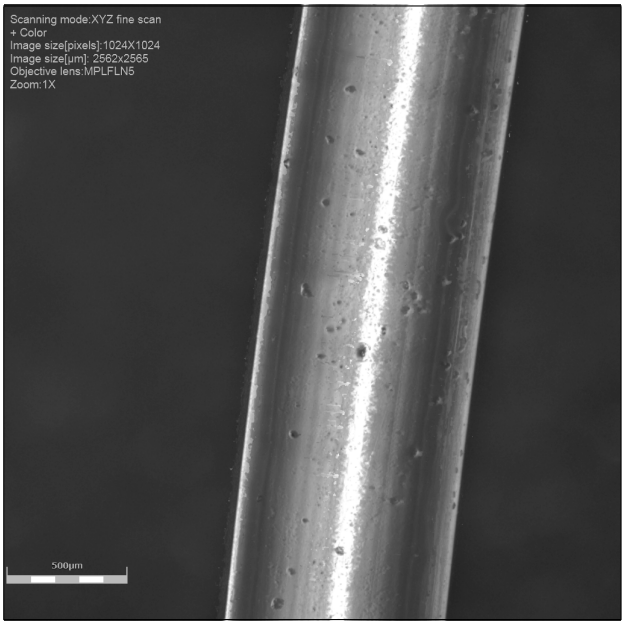

Figure 3. Wire image acquired from a laser microscope. The defects over the surface are neglected.

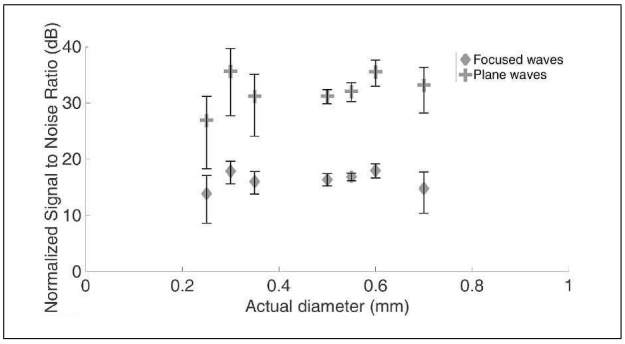

Figure 4. SNR for the different vessel diameters with the focused (diamonds) and plane wave (crosses) algorithms.

For each tube diameter, several phantoms were made, and for each phantom, a series of Doppler measurements were carried out with the probe at different positions, as explained earlier. The end-value of the calculated diameter, velocities and SNR was the average of the total number of values over 20 measurements for all diameters and for each of the Doppler algorithms.

2.7. Control of the wire diameter

To ensure that the expected and actual wire diameters were close, measurements were performed using a confocal laser scanning microscope (LEXT OLS4100, Olympus, Tokyo, Japan). For each diameter, some samples were placed flat over a uniform black paper to avoid a situation where some pixels from the background would be considered as being a part of the wires. As can be seen in the acquisition example in Figure 3, some holes and defects were highlighted. However, because the wire was carefully removed length-wise, it is assumed that the effect on the hole created inside the phantoms was negligible.

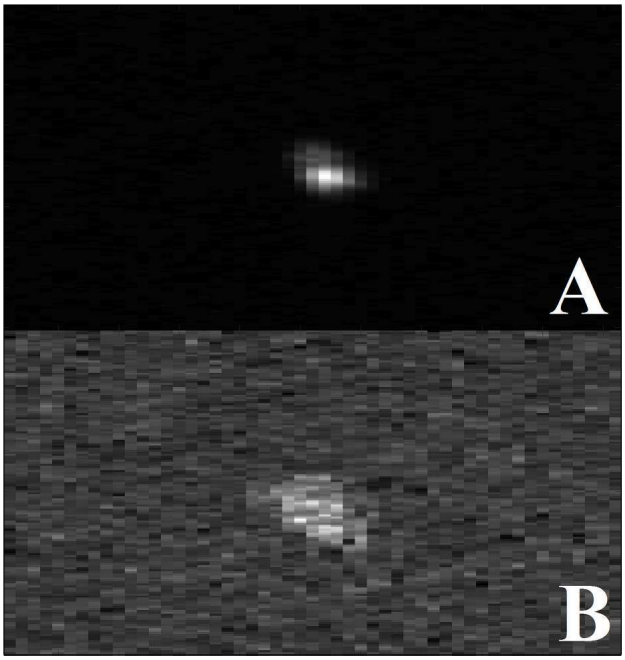

Figure 5. Reconstructed images with the plane waves (A) and focused waves (B) algorithms, acquired with the same experimental conditions. These images were trimmed from the entire original image, with the same number of pixels and centered on the flow signal. The flow diameter for these examples was 0.6 mm.

The images were firstly segmented to obtain binary values, thereby ensuring that the wire region was correctly filled. The ImageJ software was used to calculate about 5000 values captured from several images acquired per diameter in order to limit any correlation with the wire position. The actual diameters were then chosen from the maximum number of occurrences in 5 µm diameter intervals. The results summarized in Table IV show a maximum discrepancy of 0.015 mm, for an expected diameter of 0.50 mm (3%).

3. Results

3.1. Signal-to-noise ratio

The SNR calculations from the different phantoms are summarized in Figure 4. The SNR when using plane wave imaging was consistently higher than with the focused wave algorithm; it was at least 13 dB higher when using plane waves with a 0.25 mm diameter phantom and even reached up to 18 dB. It should be noted that with the smaller diameters for the focused waves, the Doppler signal was not detected in some images, leading to a mean calculation with less data versus the situation with the plane wave. This then underlines a more restrictive limitation for the depiction of the flow. The SNR differences between the two algorithms can also be observed from two reconstructed images with the same experimental conditions. An example is given in Figure 5.

3.2. Calculated diameter

Figure 6 plots the calculated diameter as compared to the theoretical wire diameter used for the phantoms, for the

Table IV. Comparison between the expected and the actual wire diameters. The maximum discrepancy is 0.015 mm (3%) for an expected diameter of 0.50 mm.

Expected diameter [mm]	0.250	0.300	0.350	0.500	0.550	0.60	0.70
Actual diameter [mm]	0.245	0.305	0.360	0.485	0.560	0.585	0.695

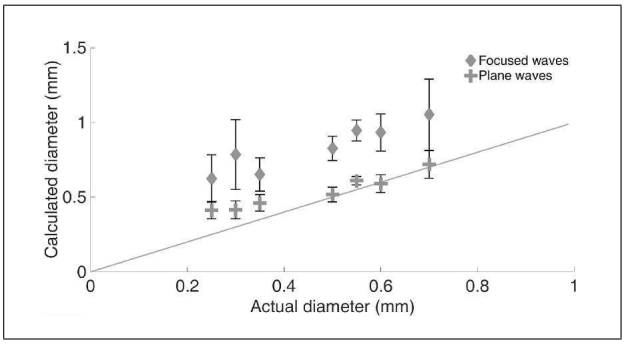

Figure 6. Calculated diameter compared to the theoretical diameter with the plane wave (crosses) and focused (diamonds) algorithms. The grey line depicts a situation where the calculated diameter and the actual diameter are identical.

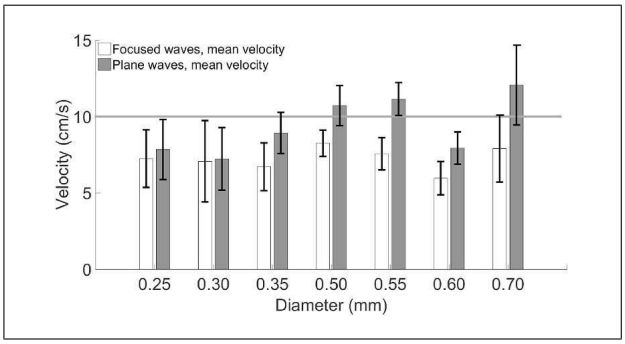

Figure 7. Mean velocity calculated for each of the phantom vessel diameters with the two algorithms. The theoretical mean velocity within the phantoms is 10 cm/s.

two algorithms and all the phantoms. While there may have been a global reduction trend in the actual diameter with the focused waves, the value was always overestimated, and could go up to more than twice the expected value for the smaller diameters. The calculated diameters from images reconstructed with plane wave emissions were close to the theoretical values for the larger vessels (0.01 mm difference for 0.6 mm and 0.7 mm diameter phantoms). The gap increased when the vessel diameter decreased. The maximum deviation was 0.16 mm for the actual value of 0.25 mm, representing a 64% error. The mean standard deviation was 0.06 mm with the plane waves sequence, compared to 0.15 mm with the focused waves sequence.

3.3. Mean velocity

The mean velocities from the ROI were also calculated using the autocorrelation calculation, and are plotted in Figure 7. With plane waves, the differences between the calculated mean velocity and the theoretical value of 10 cm/s inside the vessel ranged from −2.3 cm/s (with 0.6 mm vessel diameter phantoms) to +1.0 cm/s (with 0.55 mm diameter phantoms). The mean velocity calculated with the focused algorithm was always underestimated, with a maximum gap of 4.5 cm/s with the 0.6 mm diameter vessel phantom. The mean standard deviation was very close between the two algorithms, with values of 1.63 cm/s and 1.62 cm/s calculated from the plane waves and the focused waves sequences, respectively.

4. Discussion

Ultrasonic plane wave Doppler imaging has recently been developed to improve sensitivity and detect smaller vessels. Initially used to describe the rat brain blood flow [17]. The aim of this paper was to apply the algorithm for a spinal cord application with a wall-less phantom, considering specific conditions and limitations. For comparison, the smaller diameters studied here were in the range of the central arteries sizes reported in a human spinal cord [8]. The insonification angle was limited to 25° in order to represent surgical limitations and the narrow space available around the spinal cord following a laminectomy, limiting the probe orientation. Moreover with large angles, the whole spinal cord may not be completely included in the images with the algorithm parameters used for the experiments. Similarly, the large blood velocities in the spinal cord vessels reduce the maximum usable number of emitted waves for the plane waves Doppler imaging, so as to prevent aliasing. This corresponds to a more restrictive situation compared to the rat brain application [17].

This study showed that the calculated SNR was always higher with the plane wave algorithm for each diameter in the studied range. The 0.3 mm and 0.25 mm diameters were easily visible on images obtained with plane waves, while parts of the focused images were removed from the calculations due to undetected vessels, suggesting a limitation in a spinal cord application. These observations are confirmed from the results obtained from the rat brain imaging [17], where the authors obtained a sensitivity 5 to 30 times higher with the plane waves algorithm, with a mean of 15. Moreover, in the case of larger vessels [34], the quality of the images and the homogeneity of the Doppler signal acquired in an equivalent time for the two sequences showed a significant improvement when using the plane wave sequence. The differences are due to the low number of Doppler data with the focused waves algorithm, limiting the frequency resolution in the images.

The calculated diameters were closer to the actual value with the plane wave algorithm than with the focused one, particularly with the larger diameters. In addition, it should

be noted that the standard deviations obtained with the focused waves are almost always larger than with the plane wave's calculations, showing a higher variability in the images.

The overestimation from the focused waves data was due to vessel shape in the images, which was more variable. This can be explained by the limited precision of the Doppler signal quantification due to the limited number of images (25 images in our study). The noise was also more present and could possibly be included in the definition of the ROI. The delayed shift between two blocks can be another source contributing to the increase of the calculated diameters, as small shifts of the phantom or the probe can lead to spatial mismatch. With plane waves, the variations observed with the 0.25 mm , 0.3 mm and 0.35 mm diameter phantoms may probably be associated with the spatial resolution limitation, as these diameters are close to the theoretical value of 0.17 mm. The discrepancies observed with the 0.55 mm and 0.5 mm vessel diameter phantoms are probably linked to the acquisition process. Indeed, due to experimental limitations, a 0.6 mm diameter guide was used for these phantoms, causing possible variations as compared to the expected diameter when the wire inside the phantom was removed.

One of the main issues encountered while carrying out the measurements was the presence of cracks inside the TMM causing leakages and modifying the flow. However, this could easily be identified whenever there was no more flow from the other side of the phantom or if the water on top became cloudy, as the BMF was white. The experiments would then be stopped for that particular phantom immediately. Furthermore, the pump would deliver a specific flow to obtain a mean velocity of 10 cm/s; however the whole process could be affected by a distortion of the TMM owing to the pressure causing a small variation in the diameter cross section and then changing the velocity. This effect was assumed to be negligible for the flow calculated here.

More experiments need to be performed with plane waves in order to identify the minimum visible diameter from a plane waves Doppler ultrasound algorithm. However, technical difficulties would be encountered in such experiments, particularly in terms of avoiding vessel flow blocking with diameters smaller than a quarter of a millimeter.

5. Conclusion

The main advantage of the wall-less Doppler phantom is its reduction of artifacts, which could be caused to guide the flow by a tube. In this work, this method was used to compare the efficiency of a plane wave algorithm applied to vessels with diameters less than 1 mm which is in accordance with spinal cord vessel diameters. Some of the smallest diameters studied here, corresponding to spinal cord central arteries for humans, were not visible with focused waves. Moreover, the SNR was up to 18 dB higher with plane waves in the diameter range studied here, and the minimum tested value of 0.25 mm was easily detectable. The calculated diameters were close to the actual values when using the plane wave algorithm, allowing better anatomical identification in a real case where many vessels can be included in a restricted area of the image. Accurate measurements of the vessel diameter and velocity estimations have now opened the door to blood flow measurements.

Acknowledgements

The authors would like to aknowledge Pr. Damien Garcia and Boris Chayer, Ing., from the University of Montreal Research Center, Montreal, Qc, Canada, for their help with the signal processing and their contributions in the phantom design process. The authors also aknowledge Anthony Moulins for the laser microscope acquisitions.

References

[1] N. B. Jain, G. D. Ayers, E. N. Peterson, M. B. Harris, L. Morse, K. C. O'Connor, E. Garshick: Traumatic spinal cord injury in the United States, 1993-2012. J Am Med Assoc **313** (2015) 2236–43.

[2] N. L. Martirosyan, J. S. Feuerstein, N. Theodore, D. D. Cavalcanti, R. F. Spetzler, M. C. Preul: Blood supply and vascular reactivity of the spinal cord under normal and pathological conditions. J Neurosurg Spine **15** (2011) 238–51.

[3] M. G. Fehlings, C. H. Tator, R. D. Linden: The relationships among the severity of spinal cord injury, motor and somatosensory evoked potentials and spinal cord blood flow. Electroencephalogr Clin Neurophysiol **74** (1989) 241–59.

[4] A. Guha, C. H. Tator, J. Rochon: Spinal cord blood flow and systemic blood pressure after experimental spinal cord injury in rats. Stroke **20** (1989) 372–7.

[5] T. B. Ducker, M. Salcman, J. T. Lucas, W. B. Garrison, P. L. Perot: Experimental spinal cord trauma, II: Blood flow, tissue oxygen, evoked potentials in both paretic and plegic monkeys. Surg Neurol **10** (1978) 64–70.

[6] A. L. Goldberg, S. M. Kershah: Advances in imaging of vertebral and spinal cord injury. J Spinal Cord Med **33** (2010) 105–16.

[7] V. Rajan, B. Varghese, T. G. van Leeuwen, W. Steenbergen: Review of methodological developments in laser Doppler flowmetry. Lasers Med Sci **24** (2009) 269–83.

[8] T. H. Suh, L. Alexander: Vascular system of the human spinal cord. Arch NeurPsych **41** (1939) 659–677.

[9] G. J. Romanes: The arterial blood supply of the human spinal cord. Paraplegia **2** (1965) 199–207.

[10] T. Ohashi, T. Morimoto, K. Kawata, T. Yamada, T. Sakaki: Correlation between spinal cord blood flow and arterial diameter following acute spinal cord injury in rats. Acta Neurochir (Wien) **138** (1996) 322–9.

[11] C. A. Giller, S. S. Finn: Intraoperative measurement of spinal cord blood velocity using pulsed Doppler ultrasound. a case report. Surg Neurol **32** (1989) 387–93.

[12] J. A. Hudson, S. T. Finn-Bodner, J. R. Coates, D. C. Sorjonen, S. T. Simpson, J. C. Wright, J. E. Steiss, N. R. Cox, D. M. Vaughn, S. C. Miller, S. A. Brown, P. D. Garrett: Color Doppler imaging and Doppler spectral analysis in the spinal cord of normal dogs. Vet Radiol Ultrasound **36** (1995) 542–547.

[13] F. Abd Allah, S. Majidi, M. Watanabe, S. A. Chaudhry, A. I. Qureshi: Feasibility and validation of spinal cord vascula-

ture imaging using high resolution ultrasound. J Vasc Surg **56** (2012) 637–43.

[14] K. Shibata, S. Takamoto, Y. Kotsuka, T. Miyairi, T. Morota, K. Ueno, H. Sato: Doppler ultrasonographic identification of the critical segmental artery for spinal cord protection. Eur J Cardiothorac Surg **20** (2001) 527–32.

[15] B. Nanai, R. Lyman, P. S. Bichsel: Use of intraoperative ultrasonography in canine spinal cord lesions. Vet Radiol Ultrasound **48** (2007) 254–61.

[16] T. Tsuji, Y. Matsuyama, K. Sato, H. Iwata: Evaluation of spinal cord blood flow during prostaglandin e1-induced hypotension with power Doppler ultrasonography. Spinal Cord **39** (2001) 31–6.

[17] E. Macé, G. Montaldo, B. F. Osmanski, I. Cohen, M. Fink, M. Tanter: Functional ultrasound imaging of the brain: theory and basic principles. IEEE Trans Ultrason Ferroelectr Freq Control **60** (2013) 492–506.

[18] J. Flynn, R. Daigle, L. Pfulgrath, K. Linkhart, P. Kaczkowski: Estimation and display for vector Doppler imaging using planewave transmissions. 2011 IEEE International Ultrasonics Symposium, 2011, IEEE, 413–8.

[19] I. K. Ekroll, A. Swillens, P. Segers, T. Dahl, H. Torp, L. Lovstakken: Simultaneous quantification of flow and tissue velocities based on multi-angle plane wave imaging. IEEE Trans Ultrason Ferroelectr Freq Control **60** (2013) 727–38.

[20] B. F. Osmanski, M. Pernot, G. Montaldo, A. Bel, E. Messas, M. Tanter: Ultrafast Doppler imaging of blood flow dynamics in the myocardium. IEEE Trans Med Imaging **31** (2012) 1661–8.

[21] B. F. Osmanski, G. Montaldo, M. Tanter: Out-of-plane Doppler imaging based on ultrafast plane wave imaging. IEEE Trans Ultrason Ferroelectr Freq Control **62** (2015) 625–36.

[22] B. Denarie, T. A. Tangen, I. K. Ekroll, N. Rolim, H. Torp, T. Bjastad, L. Lovstakken: Coherent plane wave compounding for very high frame rate ultrasonography of rapidly moving targets. IEEE Trans Med Imaging **32** (2013) 1265–76.

[23] W. Dabrowski, J. Dunmore-Buyze, H. N. Cardinal, A. Fenster: A real vessel phantom for flow imaging: 3-D Doppler ultrasound of steady flow. Ultrasound Med Biol **27** (2001) 135–41.

[24] T. L. Poepping, H. N. Nikolov, M. L. Thorne, D. W. Holdsworth: A thin-walled carotid vessel phantom for Doppler ultrasound flow studies. Ultrasound Med Biol **30** (2004) 1067–78.

[25] P. Tortoli, T. Morganti, G. Bambi, C. Palombo, K. V. Ramnarine: Noninvasive simultaneous assessment of wall shear rate and wall distension in carotid arteries. Ultrasound Med Biol **32** (2006) 1661–70.

[26] E. R. Greene: Noninvasive transthoracic and transesophageal Doppler echocardiographic measurements of human coronary blood flow velocity : In vitro flow phantom validation. 2010 Annual International Conference of the IEEE Engineering in Medicine and Biology, 2010, IEEE, 3784–7.

[27] C. Veltmann, S. Lohmaier, T. Schlosser, S. Shai, A. Ehlgen, C. Pohl, H. Becher, K. Tiemann: On the design of a capillary flow phantom for the evaluation of ultrasound contrast agents at very low flow velocities. Ultrasound Med Biol **28** (2002) 625–34.

[28] D. F. Ten Cate, J. J. Luime, M. van der Ven, J. M. Hazes, K. Kooiman, N. de Jong, J. G. Bosch: Very different performance of the power Doppler modalities of several ultrasound machines ascertained by a microvessel flow phantom. Arthritis Res Ther **15** (2013) R162.

[29] R. Sakano, T. Kamishima, M. Nishida, T. Horie: Power Doppler signal calibration between ultrasound machines by use of a capillary-flow phantom for pannus vascularity in rheumatoid finger joints: a basic study. Radiol Phys Technol **8** (2015) 120–4.

[30] S. Z. Pinter, J. C. Lacefield: Detectability of small blood vessels with high-frequency power Doppler and selection of wall filter cut-off velocity for microvascular imaging. Ultrasound Med Biol **35** (2009) 1217–28.

[31] D. W. Rickey, P. A. Picot, D. A. Christopher, A. Fenster: A wall-less vessel phantom for Doppler ultrasound studies. Ultrasound Med Biol **21** (1995) 1163–76.

[32] E. L. Madsen, G. R. Frank, F. Dong: Liquid or solid ultrasonically tissue-mimicking materials with very low scatter. Ultrasound Med Biol **24** (1998) 535–42.

[33] H. Y. Ko, J. H. Park, Y. B. Shin, S. Y. Baek: Gross quantitative measurements of spinal cord segments in human. Spinal Cord **42** (2004) 35–40.

[34] J. Bercoff, G. Montaldo, T. Loupas, D. Savery, F. Mézière, M. Fink, M. Tanter: Ultrafast compound Doppler imaging: providing full blood flow characterization. IEEE Trans Ultrason Ferroelectr Freq Control. **1** (2011) 134–47.